

Moiré excitons in MoSe₂-WSe₂ heterobilayers and heterotrilayers

Michael Förg,¹ Anvar S. Baimuratov*,¹ Stanislav Yu. Kruchinin,^{2,3}
Ilia A. Vovk,⁴ Johannes Scherzer,¹ Jonathan Förste,¹ Victor Funk,¹
Kenji Watanabe,⁵ Takashi Taniguchi,⁶ and Alexander Högele*^{1,7}

¹*Fakultät für Physik, Munich Quantum Center,
and Center for NanoScience (CeNS),
Ludwig-Maximilians-Universität München,
Geschwister-Scholl-Platz 1, 80539 München, Germany*

²*Center for Computational Materials Sciences,
Faculty of Physics, University of Vienna,
Sensengasse 8/12, 1090 Vienna, Austria*

³*Nuance Communications Austria GmbH, Technologiestraße 8, 1120 Wien*

⁴*Center of Information Optical Technology,
ITMO University, Saint Petersburg 197101, Russia*

⁵*Research Center for Functional Materials,
National Institute for Materials Science,
1-1 Namiki, Tsukuba 305-0044, Japan*

⁶*International Center for Materials Nanoarchitectonics,
National Institute for Materials Science,
1-1 Namiki, Tsukuba 305-0044, Japan*

⁷*Munich Center for Quantum Science and Technology (MCQST),
Schellingstraße 4, 80799 München, Germany*

*A.S.B. email: anvar.baimuratov@lmu.de

*A.H. email: alexander.hoegel@lmu.de

Abstract

Layered two-dimensional materials exhibit rich transport and optical phenomena in twisted or lattice-incommensurate heterostructures with spatial variations of interlayer hybridization arising from moiré interference effects. Here, we report experimental and theoretical studies of excitons in twisted heterobilayers and heterotrilayers of transition metal dichalcogenides. Using MoSe₂-WSe₂ stacks as representative realizations of twisted van der Waals bilayer and trilayer heterostructures, we observe contrasting optical signatures and interpret them in the theoretical framework of interlayer moiré excitons in different spin and valley configurations. We conclude that the photoluminescence of MoSe₂-WSe₂ heterobilayer is consistent with joint contributions from radiatively decaying valley-direct interlayer excitons and phonon-assisted emission from momentum-indirect reservoirs that reside in spatially distinct regions of moiré supercells, whereas the heterotrilayer emission is entirely due to momentum-dark interlayer excitons of hybrid-layer valleys. Our results highlight the profound role of interlayer hybridization for transition metal dichalcogenide heterostacks and other realizations of multi-layered semiconductor van der Waals heterostructures.

I. INTRODUCTION

Heterostructures of layered two-dimensional materials exhibit rich transport and optical phenomena. In twisted or lattice-incommensurate heterobilayers (HBLs), laterally modulated van der Waals interactions give rise to spatial variations in the degree of interlayer hybridization on the characteristic length scale of the moiré interference pattern [1–6]. The formation of moiré superlattices has profound effects on the electronic band structure, as evidenced by the emergence of correlated transport phenomena in flat bands of twisted bilayer [7, 8] and trilayer [9, 10] graphene, or detected optically in twisted homobilayers [11] and aligned HBLs [12, 13] of transition metal dichalcogenides (TMDs). The latter also exhibit rich moiré signatures in the optical spectra of intralayer [14] and interlayer [15–18] excitons formed by Coulomb attraction among layer-locked and layer-separated electrons and holes.

In MoSe₂-WSe₂ HBL, a prominent representative of TMD heterostacks, the interlayer exciton photoluminescence (PL) is observed well below the intralayer features of monolayer MoSe₂ and WSe₂ constituents [19]. The PL energy is consistent with a staggered band alignment [20] which separates electrons and holes into the conduction and valence bands of MoSe₂ and WSe₂, respectively. In accord with layer separation, interlayer excitons exhibit

strongly prolonged radiative lifetimes [19] and reduced oscillator strength [21]. Despite numerous experimental and theoretical studies of MoSe₂-WSe₂ HBLs, the origin of the lowest energy PL remains a subject of debate [22]. While the majority of experimental studies interpret the HBL emission in terms of zero-momentum interlayer excitons with K or K' valley electrons and holes in MoSe₂ and WSe₂ [15, 16, 19, 21, 23–29], others invoke excitons built from hybridized HBL conduction band states at Q pockets [30–32], located roughly halfway between the center of the first Brillouin zone at Γ and K or K' valleys. Band structure calculations indeed suggest that hybridization of states near Q conduction band and Γ valence band of MoSe₂ and WSe₂ gives rise to strong energy renormalization upon HBL formation [2, 33, 34] which might turn either QK or $Q\Gamma$ interlayer excitons, composed of electrons at Q and holes at K or Γ , into the lowest energy states.

Additional complication arises in the presence of moiré effects. In moiré-modulated HBLs, electronic states exhibit valley-contrasting energy shifts upon interlayer hybridization, with states in K and K' valleys being less susceptible to energy reducing interactions than the conduction band states at Q or the valence band states at Γ . This effect, analogous to the origin of the direct-to-indirect band gap cross-over in TMD monolayers and bilayers [35–37], should also impact the band structure of HBLs [2] yet has been mostly neglected in the context of moiré excitons [1, 3–6]. Interlayer hybridization is expected to play an even more prominent role in heterotrilayer (HTL) systems with native homobilayers. For the explicit case of MoSe₂-WSe₂ HTLs, one would expect sizable hybridization effects between the MoSe₂ bilayer band edge states at Q and their counterparts in monolayer WSe₂, rendering the overall heterostructure an indirect band gap semiconductor.

II. RESULTS

A. MoSe₂-WSe₂ heterobilayer and heterotrilayer in cryogenic spectroscopy

Motivated by the contrasting behavior anticipated for momentum direct and indirect band edge interlayer excitons in MoSe₂-WSe₂ HBL and HTL, we performed optical spectroscopy studies of the corresponding moiré heterostructures on the same sample. The heterostack was connected to a charge-reservoir for voltage control of capacitive doping. To this end, a MoSe₂ crystal with monolayer and bilayer regions was stacked onto a WSe₂ monolayer by dry viscoelastic stamping [38], encapsulated from both sides by hexagonal boron nitride

(hBN) and stamped into contact with a gold electrode with gate voltage referenced against a grounded layer of silver capped by SiO₂ (Supplementary Note 1). The MoSe₂ crystal with a native bilayer region in 2H or AA' stacking was twisted away from parallel R-type alignment by about 4° with respect to the WSe₂ monolayer. At such relatively large angles, we expect the moiré heterostructure to be robust against reconstruction [39–41] and thus to contrast previous studies of MoSe₂-WSe₂ HBLs carefully aligned for zero twist angle in R-type stacking [24, 28] as well as moiré-free HBLs obtained from chemical vapor deposition with lattice-mismatch relaxation and inherent alignment [21, 23].

Cryogenic PL and differential reflectivity (DR) spectra of the HBL and HTL regions at 3.2 K and zero gate voltage are shown in Fig. 1a and b, respectively. The DR features in the spectral range between 1.55 eV and 1.75 eV are consistent with absorption characteristics of neutral intralayer excitons, and the vanishingly small trion feature in Fig. 1a indicates operation close to charge-neutrality (Supplementary Note 1). Whereas the two dominant DR peaks of the HBL spectrum in Fig. 1a essentially reflect the respective MoSe₂ and WSe₂ monolayer transitions around 1.6 and 1.7 eV, the HTL spectrum in Fig. 1b is different. Compared to the HBL spectrum, it exhibits a red-shift of the WSe₂ intralayer exciton peak by 8 meV because of Coulomb screening by the additional MoSe₂ layer, and a rich structure around the MoSe₂ absorption peak with possible contributions from interlayer excitons of bilayer MoSe₂ [42] as well as moiré miniband effects [6] in the twisted HTL.

Within the same energy range, the cryogenic PL is consistently dominated by intralayer excitons. Remarkably, the intralayer MoSe₂ and WSe₂ peaks in the HBL spectrum of Fig. 1a are nearly completely quenched in the HTL spectrum of Fig. 1b, indicating for the latter drastically suppressed hot luminescence due to enhanced population relaxation into lowest-energy interlayer exciton levels. This observation is in accord with the theoretical prediction of increased charge transfer efficiency via hybridized *Q* and Γ states in heterostructures [2].

Another striking difference in the PL of the heterostacks is evident in the spectra of Fig. 1a and b for interlayer excitons, with PL emission below 1.40 and 1.33 eV from HBL and HTL regions, respectively. The PL characteristics depend on the heterostack position, as confirmed by lateral displacement of the sample with respect to fixed confocal excitation and detection spots. Upon transition from the HBL to the HTL region, the set of the HTL peaks below 1.35 eV emerges at the expense of the higher energy HBL peaks with emission energy above 1.35 eV (Supplementary Note 2). At each heterostack site, the overall multi-

peak PL structure of HBL and HTL is mostly preserved upon the variation in the gate voltage (Supplementary Note 1) and excitation power down to 300 nW (Supplementary Note 3). Consistent with finite twist angle, the multi-peak PL of the HBL below 1.40 eV, with a peak separation of 30 meV between the two highest energy peaks and 15 meV between other consecutive peaks (Supplementary Note 3), is reminiscent of rich MoSe₂-WSe₂ moiré spectral features [16] rather than of simple spectra from aligned HBLs [24–29]. Remarkably, the HTL PL, with a similar peak spacing of 15 meV, is strikingly similar to the cryogenic PL from native bilayer WSe₂ [43] (Supplementary Note 4).

In time-resolved PL, HBL and HTL PL exhibit similar decay dynamics (Supplementary Note 5). Spectral sampling of the PL decay characteristics indicates the presence of at least three decay channels without conclusive dependence on the emission energy for both HBL and HTL emission. Throughout the spectral band of interlayer excitons, the PL decay exhibits three decay timescales of 3, 12 and 480 ns for HBL and 1, 12 and 300 ns for HTL. For both heterostacks, PL decay was dominated by the slow component (with a weight of 89% and 80% in HBL and HTL, respectively) with contributions of the intermediate (fast) decay channel of 8% and 13% (3% and 7%) to the HBL and HTL emission, respectively. These time scales are in accord with previous studies of MoSe₂-WSe₂ HBL [21, 31, 44, 45] and subject to different and partly competing interpretations.

B. Theory of excitons in R-stacked MoSe₂-WSe₂ heterobilayer and heterotrilayer

The differences in the PL spectra of Fig. 1a and b suggest different origins for the interlayer exciton PL in MoSe₂-WSe₂ HBL and HTL. To provide a basis for the interpretation of our observations, we performed numerical calculations of the band structure and exciton g -factors with density functional theory (DFT) in generalized gradient approximation (Supplementary Notes 6 and 7). Assuming that the twist angle is sufficiently small to employ local band structure approximation [4, 46], we restrict our analysis to three high symmetry points of the moiré superlattice in each heterostructure with stackings indicated in Fig. 2a (Supplementary Note 6). Using the band structure results from DFT, we employed the Wannier exciton model in the effective mass approximation [47] to calculate the energies of intralayer and interlayer excitons in different spin-valley configurations.

In the top panels of Fig. 2b and c we show the oscillator strength, essentially determined by the squared modulus of the coordinate operator matrix elements, for direct KK exciton

transitions in different R-type stackings of HBL and HTL. For all stackings, interlayer excitons exhibit at least two orders of magnitude lower oscillator strengths than their intralayer counterparts [33] with dipolar selection rules in agreement with the group theory analysis of R-type HBL [5, 21]. In accord with previous calculations for HBLs, we find the lowest-energy KK interlayer exciton for A'B' [4, 33] and energetically higher excitons for AA and AB' stackings. In all HBL stackings of R-type registry considered here, the lowest KK interlayer exciton is spin-like (i.e. in collinear electron spin orientation of occupied conduction band and unoccupied valence band states, and equivalent to spin-singlet configuration in the electron-hole notation), about 20 meV below its spin-unlike counterpart (or spin-triplet electron-hole pair). In AA stacking, the spin-like state has the largest oscillator strength, whereas for spin-unlike states only the KK exciton in A'B' stacking has a sizable oscillator strength in agreement with previous DFT results [33, 34].

For the HTL, our calculations predict an increase in the number of conduction bands associated with lowest energy excitons due to the additional MoSe₂ layer. As such, interlayer KK excitons can be grouped according to the localization of the conduction band electron in one of the MoSe₂ layers. For electrons localized on the MoSe₂ layer with immediate proximity to WSe₂ (full symbols in Fig. 2c), the corresponding interlayer excitons feature similar energies (with a small red-shift due to modified screening) and oscillator strengths as in the HBL system. Additional interlayer states arise from excitons with the electron localized in the upper MoSe₂ layer (open symbols in Fig. 2c). Their energetic ordering, with spin-unlike configuration again being lowest, and dipolar selection are identical to KK interlayer excitons in HBLs of H-type registry [5, 21]. However, the corresponding transitions have a drastically inhibited oscillator strengths due to a reduced wavefunction overlap between the electron and hole in the topmost MoSe₂ and the bottom WSe₂ layer and thus should not contribute sizeably to the PL of HTL [48]. Based on our analysis, we rule out excitons composed from electrons and holes that are locked in distant layers as candidates for bright PL emission in the red-most part of the HTL spectrum.

In addition to KK excitons, our calculations yield the energies of momentum-indirect QK , $Q\Gamma$ and $K\Gamma$ excitons (bottom panels of Fig. 2b and c) composed from electrons in Q (or Q') and K as well as holes at K or Γ . Note that the notion of oscillator strength is meaningless for momentum-indirect excitons without direct radiative decay pathways. The energetic ordering of interlayer excitons with zero and finite center-of-mass momentum

differs substantially in HBL and HTL systems: whereas our calculations predict energetic proximity for KK , QK and KT states in HBLs, finite-momentum QK and $Q\Gamma$ states in HTL are energetically well below the direct KK states, with an energy difference in the order of 200 meV. This trend is well known for monolayer and bilayer TMDs, where the states at K are much less sensitive to the addition of one layer than the states at Q and Γ [35–37, 49]. For the HTL, strong interlayer hybridization should result in efficient layer coupling as opposed to layer locking [48]. The respective experimental signature of enhanced relaxation from intralayer to interlayer exciton states is the strong suppression of the HTL PL around the MoSe₂ intralayer resonance at 1.62 eV in Fig. 1b.

C. Power-dependent photoluminescence and degree of circular polarization of MoSe₂-WSe₂ heterobilayer and heterotrilayer

We find experimental support for our theoretical description of HBL and HTL excitons by probing the PL and the degree of circular polarization (P_C) as a function of excitation power. The corresponding results are shown in Fig. 3a, b and c, d for HBL and HTL, respectively. Upon increasing excitation power from 0.1 to 100 μW , the HBL spectrum develops a pronounced shoulder above 1.40 eV with vanishing P_C (indicated by the dashed black line in Fig. 3a and b). This feature is consistent with hot luminescence from energetically higher states with z -polarized in-plane emission collected by our objective with high numerical aperture and corresponding collection solid angle. Our theory provides spin-unlike and spin-like interlayer excitons in AA and A'B' stacking, respectively, as two potential reservoirs for this emission (z -polarized states in Fig. 2b).

In contrast, the brightest HBL peaks between 1.32 and 1.40 eV with a positive degree of circular polarization are present down to lowest excitation powers. They are consistent with spin-like (spin-unlike) KK interlayer excitons in AA (A'B') stacking (states in Fig. 2b with σ^+ polarization). As we observe no sign reversal in P_C as expected for the lowest-energy spin-like KK interlayer exciton in A'B' stacking (state in Fig. 2b with σ^- polarization) and reported previously for structured HBL PL [16], strong contribution from A'B' stacking is unlikely in our sample. This implies that AA domains dominate the HBL PL in rigid moiré supercells, although A'B' regions should be at least of comparable size [39]. In the presence of reconstruction, one would expect predominance of energetically favored A'B' and AB'

triangular domains of comparable area [39, 40, 50]. Without reconstruction, on the other hand, a reversal in the energetic ordering of AA and A'B' interlayer excitons at finite twist angles, as predicted recently by theory for R-type MoSe₂-WSe₂ heterostructures [51], would satisfactorily explain the observation.

According to our theory analysis, the structure of HTL PL is of different origin. The HTL data in Fig. 3c and d reveal *KK* interlayer exciton states through power-activated hot luminescence at the higher-energy side of the spectrum with finite circular degrees of polarization (indicated by the dashed red lines in Fig. 3c and d). The respective emission peaks at 1.35 and 1.38 eV can be ascribed to *KK* interlayer excitons with σ^+ polarization in (A'B')A' or (AA)A' stackings (red-colored states in Fig. 2c). Similar to the HBL, the HTL spectrum exhibits upon 100 μ W excitation power an additional higher-energy hot luminescence peak at 1.43 eV with vanishing P_C (black dashed line in Fig. 3c and d). The respective candidate from theory is the *KK* reservoir in (AB')A' stacking with z -polarized transition, as the (AA)A' interlayer excitons with the same selection rules are dismissed due to vanishingly small oscillator strength (black-colored states in Fig. 2c). On the low energy side, the peaks around 1.30 eV below the energy of *KK* hot-luminescence can result as phonon sidebands from momentum-dark *QK* or *Q Γ* interlayer exciton reservoirs (states in the bottom panel of Fig. 2c shown in green and orange). Without removing the ambiguity in the assignment of the lowest-energy reservoir to *QK* or *Q Γ* , this scenario explains the similarity in the spectral shape of HTL PL and the PL of native bilayer WSe₂ originating from momentum-indirect excitons [43, 52].

D. Magneto-luminescence of MoSe₂-WSe₂ heterobilayer and heterotrilinear

Additional insight into the origin of HBL and HTL peaks is obtained from magneto-luminescence experiments in Faraday configuration and theoretical analysis. The experimental dispersion of the PL peaks in external magnetic field applied perpendicular to the heterostructure is shown in Fig. 4. The solid black lines indicate linear energy shifts recorded for σ^+ and σ^- circularly polarized PL as a function of magnetic field. From this set of data, we determine the respective g -factors using the relation $\Delta E = g\mu_B B$, where ΔE is the energy splitting between σ^+ and σ^- polarized peaks proportional to the interlayer exciton g -factor, μ_B is the Bohr magneton, and B is the magnetic field. For the HBL, the extracted g -factors

range between -4.2 and -6.2 with the same sign as for WSe_2 intralayer excitons, whereas the HTL peaks exhibit g -factors between -12 and -13 . In combination with observations described above and ab-initio calculations of g -factors for various spin-valley configurations of interlayer excitons in high-symmetry HBL and HTL stackings (Supplementary Note 7), these values suggest the following picture for MoSe_2 - WSe_2 HBL and HTL stacks twisted away from ideal R-type registry.

III. DISCUSSION

First, we note that the experimental g -factors determined for the HBL peaks from the data of Fig. 4a and b (-6.2 ± 0.8 , -4.2 ± 0.8 and -5.5 ± 0.8) are consistent with previous studies of aligned MoSe_2 - WSe_2 heterostructures in R-type registry with absolute values in the range from 6.1 to 8.5 [15, 24, 28]. They clearly contrast the interlayer exciton g -factor values between 15 and 16 in HBLs of H-type registry [15, 26, 29, 53]. For the respective KK interlayer excitons in R-type HBLs, our calculations (Supplementary Note 7) predict an absolute g -factor value close to 6 and opposite signs for the degrees of circular polarization in AA and A'B' stackings (with negative and positive P_C , respectively), in agreement with a similar theoretical analysis of interlayer exciton g -factor values and signs [54, 55].

We proceed by discussing possible origins of the structured HBL emission. In the framework of moiré excitons, multi-peak PL has been ascribed to interlayer exciton states confined in moiré quantum wells [16, 45]. Assuming that finite twist indeed reverses the energetic ordering of interlayer excitons in A'B' and AA stackings [51], the pronounced peaks of HBL PL below 1.40 eV with positive P_C and negative g -factors in the order of -6 would correspond to quantum well states of zero-momentum KK moiré excitons in AA stacked regions. This interpretation, however, is only plausible if the redistribution of interlayer exciton population among moiré quantum well sub-bands is bottlenecked. In the presence of population relaxation and thermal redistribution on timescales of the order or below 100 – 300 ns (longest decay components in PL), one would expect the PL from quantum well excited states to disappear or at least to diminish in intensity due to insufficient exciton population at low excitation powers and low temperature. Instead, we always find the highest energy peak to exhibit the highest intensity down to lowest excitation powers.

An alternative interpretation invokes KK interlayer excitons trapped in disorder potentials. Within this scenario, the highest energy peak would stem from KK excitons in AA stacked regions decaying via their respective σ^+ polarized radiative channel on the timescale of a few nanoseconds, whereas lower energy peaks with similar g -factors and P_C would reflect the respective defect-bound states with prolonged lifetimes. This scenario, however, is in conflict with the observation of spectrally independent PL decay, dismissing defect-trapped interlayer excitons with reduced energy as the primary source of the structured PL. The scenario of an energetically homogeneous distribution of localization by disorder over the entire spectral emission window seems even less plausible.

Finally, the multi-peak structure of HBL PL can be attributed to the joint emission from zero-momentum and finite-momentum interlayer exciton reservoirs [21, 31]. In addition to spin-like KK excitons with a g -factor of 6, our theory identifies spin-like $K\Gamma$ and spin-unlike $Q'\Gamma$ with respective g -factors of 4 and 5 as candidates for the lower-energy HBL peaks. Note that theory finds these states in close energetic proximity to spin- and momentum-bright KK interlayer excitons (Fig. 2b). In this framework, the corresponding HBL peaks would qualify as phonon sidebands of $K\Gamma$ or $Q'\Gamma$ (or both), and the peak spacings of 30 and 15 meV would reflect the energies of optical and acoustic phonons, or higher-order combinations thereof [21, 43]. This, however, holds only for staggered A'B' and AB' stackings that favor energy-reducing layer hybridization among the conduction band states around Q and Q' and the valence band states in the center of the Brillouin zone at Γ . In contrast, hybridization is less effective in AA-stacked regions, upshifting the energies of $K\Gamma$ and $Q'\Gamma$ manifolds away from KK interlayer and towards intralayer excitons of MoSe₂ and WSe₂ (two highest-energy states in the bottom panel of Fig. 2b). Remarkably, this setting predicts the contributions of zero-momentum and finite-momentum interlayer excitons to HBL PL to stem from different stackings and thus from spatially distinct reservoirs. Consequently, the two-dimensional landscape of lowest-energy moiré excitons would thus be shaped by momentum-direct and indirect states residing in spatially separated domains of different stackings.

The scenario is more simple for HTL PL with finite-momentum excitons being lowest in energy. For the peaks of Fig. 4c and d, the absolute values of g -factors of about 12 take momentum-direct KK interlayer excitons as well as momentum-indirect reservoirs $K\Gamma$ and $Q\Gamma$ out of the picture. Among the former, dipole-active KK states disqualify due to their g -factor of ~ 6 , and KK spin-like (spin-unlike) configurations formed by the electron in

the lower (upper) MoSe₂ layer with theoretical g -factors between 11 and 13, as well as the respective $K'K$ counterparts with similar g -factors, are dismissed due to higher energies and thus negligibly small exciton populations. The latter momentum-indirect $K\Gamma$ and $Q\Gamma$ states exhibit only small g -factors because of the vanishing valley Zeeman term in the Γ valley. By exclusion, the experimentally observed g -factors identify spin-like QK and spin-unlike $Q'K$ interlayer excitons with theoretical g -factors of ~ 10 and 14 as the only reasonable sources for the HTL PL peaks in the form of phonon sidebands.

From the perspective of moiré exciton energy landscape governed by interlayer hybridization, lowest-energy HBL and HTL excitons should not differ in their spin-valley composition. Our analysis, however, suggests spin-like $K\Gamma$ or spin-unlike $Q'\Gamma$ states in HBL, and spin-like QK or spin-unlike $Q'K$ states in HTL as lowest-energy manifolds. This controversy indicates that effects beyond hybridization have to be taken into account: the interplay of laterally modulated strain in moiré landscapes with opposite energy shifts for K versus Q and Γ valleys [56], and the combined piezoelectric and ferroelectric effects in the order of tens of meV [51] acting differently on interlayer excitons of distinct spin-valley configurations can reorder the hierarchy of energetically proximal interlayer exciton states.

In conclusion, our experimental and theoretical study of excitons in twisted MoSe₂-WSe₂ HBL and HTL of R-type registry promote a complex picture of HBL PL. It is consistent with radiative recombination of zero-momentum KK interlayer excitons and phonon-assisted emission from momentum-indirect reservoirs residing in spatially distinct regions of high-symmetry stackings. In contrast, the emission from the respective HTL system is entirely governed by phonon-assisted decay of momentum-dark QK or $Q'K$ interlayer excitons. We base our conclusions on extensive optical spectroscopy experiments and calculations of the band structures, exciton states and g -factors for MoSe₂-WSe₂ HBL and HTL close to R-type registry. On these specific realizations of MoSe₂-WSe₂ heterostacks, our results highlight the primary role of moiré-modulated interlayer hybridization for the relaxation and formation of excitons in twisted van der Waals heterostructures with increasing layer number and structural complexity. Despite the extensive work presented here, a complete understanding of the rich phenomena observed in TMD heterostructures of different registries and alignment angles will require more efforts in experiment and theory to include piezoelectric and ferroelectric effects as well as strain at a detailed, quantitative level, and in the presence of reconstruction effects.

Methods:

The field-effect device based on a MoSe₂-WSe₂ heterostructure was fabricated by hot pick-up technique [38]. First, a layer of hBN was picked up, followed by MoSe₂ with ML and BL regions, a ML of WSe₂ and a capping layer of hBN. The heterostack was subsequently placed in contact to a gold electrode that was deposited on a silver-coated glass substrate with a SiO₂ capping layer of 60 nm. PL and DR experiments were performed in a home-built cryogenic microscope. The sample was mounted on piezo-stepping and scanning units (attocube systems, ANPxy101, ANPz101 and ANSxy100) for positioning with respect to a low-temperature objective (attocube systems, LT-APO/LWD/NIR/0.63 or LT-APO/NIR/0.81). The microscope was placed in a dewar with an inert helium atmosphere at a pressure of 20 mbar and immersed in liquid helium at 4.2 K or operated at 3.2 K in a closed-cycle cryostat (attocube systems, attoDRY1000) equipped with a solenoid for magnetic fields of up to ± 9 T. DR experiments were performed with a wavelength-tunable supercontinuum laser (NKT, SuperK Extreme or SuperK Varia), also used for PL excitation around 633 or 715 nm with repetition rates down to 2 MHz. For continuous-wave measurements, the PL was excited with a laser diode at 635 nm or a HeNe laser, spectrally dispersed by a monochromator (Roper Scientific, Acton SP 2750, SP 2558 or Acton SpectraPro 300i) and recorded with a nitrogen-cooled silicon CCD (Roper Scientific, PyLoN or Spec-10:100BR) or thermo-electrically cooled CCD (Andor iDus). Time-resolved PL was detected with an avalanche photodiode (Excelitas SPCM-AQRH) and correlated with a single photon counting system (PicoQuant, PicoHarp 300).

Data availability:

The data that support the findings of this study are available from the corresponding authors upon reasonable request.

REFERENCES

- [1] F. Wu, T. Lovorn, and A. H. MacDonald, Topological exciton bands in moiré heterojunctions, *Phys. Rev. Lett.* **118**, 147401 (2017).
- [2] Y. Wang, Z. Wang, W. Yao, G.-B. Liu, and H. Yu, Interlayer coupling in commensurate and incommensurate bilayer structures of transition-metal dichalcogenides, *Phys. Rev. B* **95**, 115429 (2017).
- [3] H. Yu, G.-B. Liu, J. Tang, X. Xu, and W. Yao, Moiré excitons: From programmable quantum emitter arrays to spin-orbit-coupled artificial lattices, *Sci. Adv.* **3**, e1701696 (2017).
- [4] F. Wu, T. Lovorn, and A. H. MacDonald, Theory of optical absorption by interlayer excitons in transition metal dichalcogenide heterobilayers, *Phys. Rev. B* **97**, 035306 (2018).
- [5] H. Yu, G.-B. Liu, and W. Yao, Brightened spin-triplet interlayer excitons and optical selection rules in van der Waals heterobilayers, *2D Mater.* **5**, 035021 (2018).
- [6] D. A. Ruiz-Tijerina and V. I. Fal’ko, Interlayer hybridization and moiré superlattice minibands for electrons and excitons in heterobilayers of transition-metal dichalcogenides, *Phys. Rev. B* **99**, 125424 (2019).
- [7] Y. Cao, V. Fatemi, A. Demir, S. Fang, S. L. Tomarken, J. Y. Luo, J. D. Sanchez-Yamagishi, K. Watanabe, T. Taniguchi, E. Kaxiras, R. C. Ashoori, and P. Jarillo-Herrero, Correlated insulator behaviour at half-filling in magic-angle graphene superlattices, *Nature* **556**, 80 (2018).
- [8] Y. Cao, V. Fatemi, S. Fang, K. Watanabe, T. Taniguchi, E. Kaxiras, and P. Jarillo-Herrero, Unconventional superconductivity in magic-angle graphene superlattices, *Nature* **556**, 43 (2018).
- [9] G. Chen, L. Jiang, S. Wu, B. Lyu, H. Li, B. L. Chittari, K. Watanabe, T. Taniguchi, Z. Shi, J. Jung, Y. Zhang, and F. Wang, Evidence of a gate-tunable mott insulator in a trilayer graphene moiré superlattice, *Nat. Phys.* **15**, 237 (2019).
- [10] G. Chen, A. L. Sharpe, P. Gallagher, I. T. Rosen, E. J. Fox, L. Jiang, B. Lyu, H. Li, K. Watanabe, T. Taniguchi, J. Jung, Z. Shi, D. Goldhaber-Gordon, Y. Zhang, and F. Wang, Signatures of tunable superconductivity in a trilayer graphene moiré superlattice, *Nature* **572**, 215 (2019).
- [11] Y. Shimazaki, I. Schwartz, K. Watanabe, T. Taniguchi, M. Kroner, and A. Imamoglu, Strongly

- correlated electrons and hybrid excitons in a moiré heterostructure, *Nature* **580**, 472 (2020).
- [12] Y. Tang, L. Li, T. Li, Y. Xu, S. Liu, K. Barmak, K. Watanabe, T. Taniguchi, A. H. MacDonald, J. Shan, and K. F. Mak, Simulation of Hubbard model physics in WSe_2/WS_2 moiré superlattices, *Nature* **579**, 353 (2020).
- [13] E. C. Regan, D. Wang, C. Jin, M. I. Bakti Utama, B. Gao, X. Wei, S. Zhao, W. Zhao, Z. Zhang, K. Yumigeta, M. Blei, J. D. Carlström, K. Watanabe, T. Taniguchi, S. Tongay, M. Crommie, A. Zettl, and F. Wang, Mott and generalized Wigner crystal states in WSe_2/WS_2 moiré superlattices, *Nature* **579**, 359 (2020).
- [14] N. Zhang, A. Surrente, M. Baranowski, D. K. Maude, P. Gant, A. Castellanos-Gomez, and P. Plochocka, Moiré Intralayer Excitons in a $\text{MoSe}_2/\text{MoS}_2$ Heterostructure, *Nano Lett.* **18**, 7651 (2018).
- [15] K. L. Seyler, P. Rivera, H. Yu, N. P. Wilson, E. L. Ray, D. G. Mandrus, J. Yan, W. Yao, and X. Xu, Signatures of moiré-trapped valley excitons in $\text{MoSe}_2/\text{WSe}_2$ heterobilayers, *Nature* **567**, 66 (2019).
- [16] K. Tran, G. Moody, F. Wu, X. Lu, J. Choi, K. Kim, A. Rai, D. A. Sanchez, J. Quan, A. Singh, J. Embley, A. Zepeda, M. Campbell, T. Autry, T. Taniguchi, K. Watanabe, N. Lu, S. K. Banerjee, K. L. Silverman, S. Kim, E. Tutuc, L. Yang, A. H. MacDonald, and X. Li, Evidence for moire excitons in van der waals heterostructures, *Nature* **567**, 71 (2019).
- [17] C. Jin, E. C. Regan, A. Yan, M. I. B. Utama, D. Wang, S. Zhao, Y. Qin, S. Yang, Z. Zheng, S. Shi, K. Watanabe, T. Taniguchi, S. Tongay, A. Zettl, and F. Wang, Observation of moiré excitons in WSe_2/WS_2 heterostructure superlattices, *Nature* **567**, 76 (2019).
- [18] E. M. Alexeev, D. A. Ruiz-Tijerina, M. Danovich, M. J. Hamer, D. J. Terry, P. K. Nayak, S. Ahn, S. Pak, J. Lee, J. I. Sohn, M. R. Molas, M. Koperski, K. Watanabe, T. Taniguchi, K. S. Novoselov, R. V. Gorbachev, H. S. Shin, V. I. Fal’ko, and A. I. Tartakovskii, Resonantly hybridized excitons in moiré superlattices in van der Waals heterostructures, *Nature* **567**, 81 (2019).
- [19] P. Rivera, S. John R., A. M. Jones, J. S. Ross, S. Wu, G. Aivazian, P. Klement, K. Seyler, G. Clark, N. J. Ghimire, J. Yan, D. G. Mandrus, W. Yao, and X. Xu, Observation of long-lived interlayer excitons in monolayer MoSe_2 - WSe_2 heterostructures, *Nat. Commun.* **6**, 6242 (2015).
- [20] J. Kang, S. Tongay, J. Zhou, J. Li, and J. Wu, Band offsets and heterostructures of two-

- dimensional semiconductors, *Appl. Phys. Lett.* **102**, 012111 (2013).
- [21] M. Förg, L. Colombier, R. K. Patel, J. Lindlau, A. D. Mohite, H. Yamaguchi, M. M. Glazov, D. Hunger, and A. Högele, Cavity-control of interlayer excitons in van der waals heterostructures, *Nat. Commun.* **10**, 3697 (2019).
- [22] T. Deilmann, M. Rohlfing, and U. Wurstbauer, Light-matter interaction in van der waals hetero-structures, *J. Phys. Condens. Matter* **32**, 333002 (2020).
- [23] W.-T. Hsu, L.-S. Lu, P.-H. Wu, M.-H. Lee, P.-J. Chen, P.-Y. Wu, Y.-C. Chou, H.-T. Jeng, L.-J. Li, M.-W. Chu, and W.-H. Chang, Negative circular polarization emissions from WSe₂/MoSe₂ commensurate heterobilayers, *Nat. Commun.* **9**, 1356 (2018).
- [24] A. Ciarrocchi, D. Unuchek, A. Avsar, K. Watanabe, T. Taniguchi, and A. Kis, Polarization switching and electrical control of interlayer excitons in two-dimensional van der waals heterostructures, *Nat. Photon.* **13**, 131 (2019).
- [25] L. Zhang, R. Gogna, G. W. Burg, J. Horng, E. Paik, Y.-H. Chou, K. Kim, E. Tutuc, and H. Deng, Highly valley-polarized singlet and triplet interlayer excitons in van der waals heterostructure, *Phys. Rev. B* **100**, 041402 (2019).
- [26] T. Wang, S. Miao, Z. Li, Y. Meng, Z. Lu, Z. Lian, M. Blei, T. Taniguchi, K. Watanabe, S. Tongay, D. Smirnov, and S.-F. Shi, Giant Valley-Zeeman Splitting from Spin-Singlet and Spin-Triplet Interlayer Excitons in WSe₂/MoSe₂ Heterostructure, *Nano Lett.* **20**, 694 (2020).
- [27] E. V. Calman, L. H. Fowler-Gerace, D. J. Choksy, L. V. Butov, D. E. Nikonov, I. A. Young, S. Hu, A. Mishchenko, and A. K. Geim, Indirect Excitons and Trions in MoSe₂/WSe₂ van der Waals Heterostructures, *Nano Lett.* **20**, 1869 (2020).
- [28] A. Y. Joe, L. A. Jauregui, K. Pistunova, Z. Lu, D. S. Wild, G. Scuri, K. D. Greve, R. J. Gelly, Y. Zhou, J. Sung, A. M. Valdivia, A. Sushko, K. Watanabe, D. Smirnov, M. D. Lukin, H. Park, and P. Kim, Electrically controlled emission from triplet charged excitons in atomically thin heterostructures, [arXiv:1912.07678](https://arxiv.org/abs/1912.07678).
- [29] A. Delhomme, D. Vaclavkova, A. Slobodeniuk, M. Orlita, M. Potemski, D. M. Basko, K. Watanabe, T. Taniguchi, D. Mauro, C. Barreateau, E. Giannini, A. F. Morpurgo, N. Ubrig, and C. Faugeras, Flipping exciton angular momentum with chiral phonons in MoSe₂/WSe₂ heterobilayers, *2D Mater.* **7**, 041002 (2020).
- [30] P. K. Nayak, Y. Horbatenko, S. Ahn, G. Kim, J.-U. Lee, K. Y. Ma, A.-R. Jang, H. Lim, D. Kim, S. Ryu, H. Cheong, N. Park, and H. S. Shin, Probing Evolution of Twist-Angle

- Dependent Interlayer Excitons in MoSe₂/WSe₂ van der Waals Heterostructures, *ACS Nano* **11**, 4041 (2017).
- [31] B. Miller, A. Steinhoff, B. Pano, J. Klein, F. Jahnke, A. Holleitner, and U. Wurstbauer, Long-Lived Direct and Indirect Interlayer Excitons in van der Waals Heterostructures, *Nano Lett.* **17**, 5229 (2017).
- [32] A. T. Hanbicki, H.-J. Chuang, M. R. Rosenberger, C. S. Hellberg, S. V. Sivaram, K. M. McCreary, I. I. Mazin, and B. T. Jonker, Double Indirect Interlayer Exciton in a MoSe₂/WSe₂ van der Waals Heterostructure, *ACS Nano* **12**, 4719 (2018).
- [33] R. Gillen and J. Maultzsch, Interlayer excitons in MoSe₂/WSe₂ heterostructures from first principles, *Phys. Rev. B* **97**, 165306 (2018).
- [34] E. Torun, H. P. C. Miranda, A. Molina-Sánchez, and L. Wirtz, Interlayer and intralayer excitons in MoS₂/WS₂ and MoSe₂/WSe₂ heterobilayers, *Phys. Rev. B* **97**, 245427 (2018).
- [35] A. Splendiani, L. Sun, Y. Zhang, T. Li, J. Kim, C.-Y. Chim, G. Galli, and F. Wang, Emerging Photoluminescence in Monolayer MoS₂, *Nano Lett.* **10**, 1271 (2010).
- [36] K. F. Mak, C. Lee, J. Hone, J. Shan, and T. F. Heinz, Atomically Thin MoS₂: A New Direct-Gap Semiconductor, *Phys. Rev. Lett.* **105**, 136805 (2010).
- [37] G.-B. Liu, D. Xiao, Y. Yao, X. Xu, and W. Yao, Electronic structures and theoretical modelling of two-dimensional group-vib transition metal dichalcogenides, *Chem. Soc. Rev.* **44**, 2643 (2015).
- [38] F. Pizzocchero, L. Gammelgaard, B. S. Jessen, J. M. Caridad, L. Wang, J. Hone, P. Bøggild, and T. J. Booth, The hot pick-up technique for batch assembly of van der Waals heterostructures, *Nat. Commun.* **7**, 11894 (2016).
- [39] S. Carr, D. Massatt, S. B. Torrisi, P. Cazeaux, M. Luskin, and E. Kaxiras, Relaxation and domain formation in incommensurate two-dimensional heterostructures, *Phys. Rev. B* **98**, 224102 (2018).
- [40] V. V. Enaldiev, V. Zólyomi, C. Yelgel, S. J. Magorrian, and V. I. Fal'ko, Stacking domains and dislocation networks in marginally twisted bilayers of transition metal dichalcogenides, *Phys. Rev. Lett.* **124**, 206101 (2020).
- [41] J. Holler, S. Meier, M. Kempf, P. Nagler, K. Watanabe, T. Taniguchi, T. Korn, and C. Schüller, Low-frequency raman scattering in WSe₂-MoSe₂ heterobilayers: Evidence for atomic reconstruction, *Appl. Phys. Lett.* **117**, 013104 (2020).

- [42] J. Horng, T. Stroucken, L. Zhang, E. Y. Paik, H. Deng, and S. W. Koch, Observation of interlayer excitons in MoSe₂ single crystals, *Phys. Rev. B* **97**, 241404 (2018).
- [43] J. Lindlau, M. Selig, A. Neumann, L. Colombier, J. Förste, V. Funk, M. Förg, J. Kim, G. Berghäuser, T. Taniguchi, K. Watanabe, F. Wang, E. Malic, and A. Högele, The role of momentum-dark excitons in the elementary optical response of bilayer WSe₂, *Nat. Commun.* **9**, 2586 (2018).
- [44] C. Jiang, W. Xu, A. Rasmita, Z. Huang, K. Li, Q. Xiong, and W.-b. Gao, Microsecond dark-exciton valley polarization memory in two-dimensional heterostructures, *Nat. Commun.* **9**, 753 (2018).
- [45] J. Choi, M. Florian, A. Steinhoff, D. Erben, K. Tran, D. S. Kim, L. Sun, J. Quan, R. Claassen, S. Majumder, J. A. Hollingsworth, T. Taniguchi, K. Watanabe, K. Ueno, A. Singh, G. Moody, F. Jahnke, and X. Li, Twist angle-dependent interlayer exciton lifetimes in van der waals heterostructures, *Phys. Rev. Lett.* **126**, 047401 (2021).
- [46] H. Yu, Y. Wang, Q. Tong, X. Xu, and W. Yao, Anomalous light cones and valley optical selection rules of interlayer excitons in twisted heterobilayers, *Phys. Rev. Lett.* **115**, 187002 (2015).
- [47] G. Berghäuser and E. Malic, Analytical approach to excitonic properties of MoS₂, *Phys. Rev. B* **89**, 125309 (2014).
- [48] M. Brotons-Gisbert, H. Baek, A. Molina-Sánchez, A. Campbell, E. Scerri, D. White, K. Watanabe, T. Taniguchi, C. Bonato, and B. D. Gerardot, Spin-layer locking of interlayer excitons trapped in moiré potentials, *Nat. Mater.* **19**, 630 (2020).
- [49] T. Deilmann and K. S. Thygesen, Finite-momentum exciton landscape in mono- and bilayer transition metal dichalcogenides, *2D Mater.* **6**, 035003 (2019).
- [50] A. Weston, Y. Zou, V. Enaldiev, A. Summerfield, N. Clark, V. Zólyomi, A. Graham, C. Yelgel, S. Magorrian, M. Zhou, J. Zultak, D. Hopkinson, A. Barinov, T. H. Bointon, A. Kretinin, N. R. Wilson, P. H. Beton, V. I. Fal’ko, S. J. Haigh, and R. Gorbachev, Atomic reconstruction in twisted bilayers of transition metal dichalcogenides, *Nat. Nanotechnol.* **15**, 592 (2020).
- [51] V. Enaldiev, F. Ferreira, S. Magorrian, and V. I. Fal’ko, Piezoelectric networks and ferroelectric domains in twistrionic superlattices in WS₂/MoS₂ and WSe₂/MoSe₂ bilayers, *2D Materials* (2021).
- [52] J. Förste, N. V. Tepliakov, S. Yu. Kruchinin, J. Lindlau, V. Funk, M. Förg, K. Watanabe,

- T. Taniguchi, A. S. Baimuratov, and A. Högele, Exciton g -factors in monolayer and bilayer WSe₂ from experiment and theory, *Nat. Commun.* **11**, 4539 (2020).
- [53] P. Nagler, M. V. Ballottin, A. A. Mitioglu, F. Mooshammer, N. Paradiso, C. Strunk, R. Huber, A. Chernikov, P. C. Christianen, C. Schüller, and T. Korn, Giant magnetic splitting inducing near-unity valley polarization in van der Waals heterostructures, *Nat. Commun.* **8**, 1551 (2017).
- [54] T. Woźniak, P. E. Faria Junior, G. Seifert, A. Chaves, and J. Kunstmann, Exciton g factors of van der waals heterostructures from first-principles calculations, *Phys. Rev. B* **101**, 235408 (2020).
- [55] F. Xuan and S. Y. Quek, Valley zeeman effect and landau levels in two-dimensional transition metal dichalcogenides, *Phys. Rev. Research* **2**, 033256 (2020).
- [56] O. B. Aslan, M. Deng, M. L. Brongersma, and T. F. Heinz, Strained bilayer WSe₂ with reduced exciton-phonon coupling, *Phys. Rev. B* **101**, 115305 (2020).

Competing interests:

The authors declare no competing interests.

Acknowledgements:

This research was funded by the European Research Council (ERC) under the Grant Agreement No. 772195 as well as the Deutsche Forschungsgemeinschaft (DFG, German Research Foundation) within the Priority Programme SPP 2244 "2DMP" and the Germany's Excellence Strategy EXC-2111-390814868. Theoretical work was financially supported by the Foundation for the Advancement of Theoretical Physics and Mathematics "BASIS". A. S. B. has received funding from the European Union's Framework Programme for Research and Innovation Horizon 2020 (2014–2020) under the Marie Skłodowska-Curie Grant Agreement No. 754388, and from LMU Munich's Institutional Strategy LMUexcellent within the framework of the German Excellence Initiative (No. ZUK22). S. Yu. K. acknowledges support from the Austrian Science Fund (FWF) within the Lise Meitner Project No. M 2198-N30, and A. H. from the Center for NanoScience (CeNS) and the LMUinnovativ project Functional Nanosystems (FuNS). K. W. and T. T. acknowledge support from the Elemental Strategy Initiative conducted by the MEXT, Japan, Grant Number JPMXP0112101001, JSPS KAKENHI Grant Numbers JP20H00354 and the CREST(JPMJCR15F3), JST.

Contributions:

M. F., J. S., J. F., and V. F. fabricated samples with high-quality hBN provided by K. W. and T. T. and performed experiments; M. F., A. S. B. and A. H. analyzed the data; A. S. B. developed theoretical concepts and performed calculations; I. A. V., S. Yu. K. performed numerical calculations; M. F., A. S. B. and A. H. prepared the figures and wrote the manuscript. All authors commented on the manuscript.

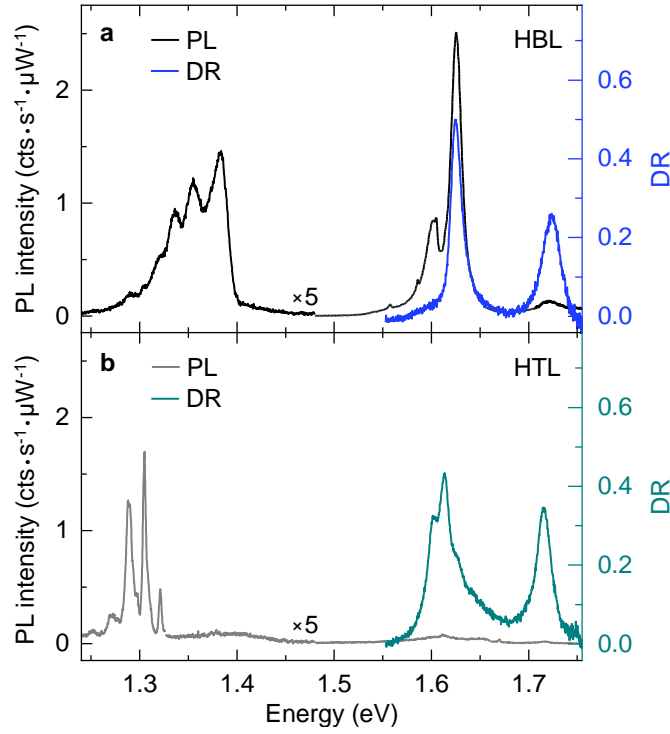


FIG. 1. Cryogenic photoluminescence and differential reflectivity spectra of MoSe_2 - WSe_2 heterobilayer and heterotrilinear. **a** and **b**, Photoluminescence (black and grey) and differential reflectivity (blue and dark cyan) spectra of twisted HBL and HTL MoSe_2 - WSe_2 at 3.2 K. The luminescence was excited with linearly polarized excitation laser at 1.85 eV and scaled in intensity below 1.47 eV by a factor of 5 in both graphs.

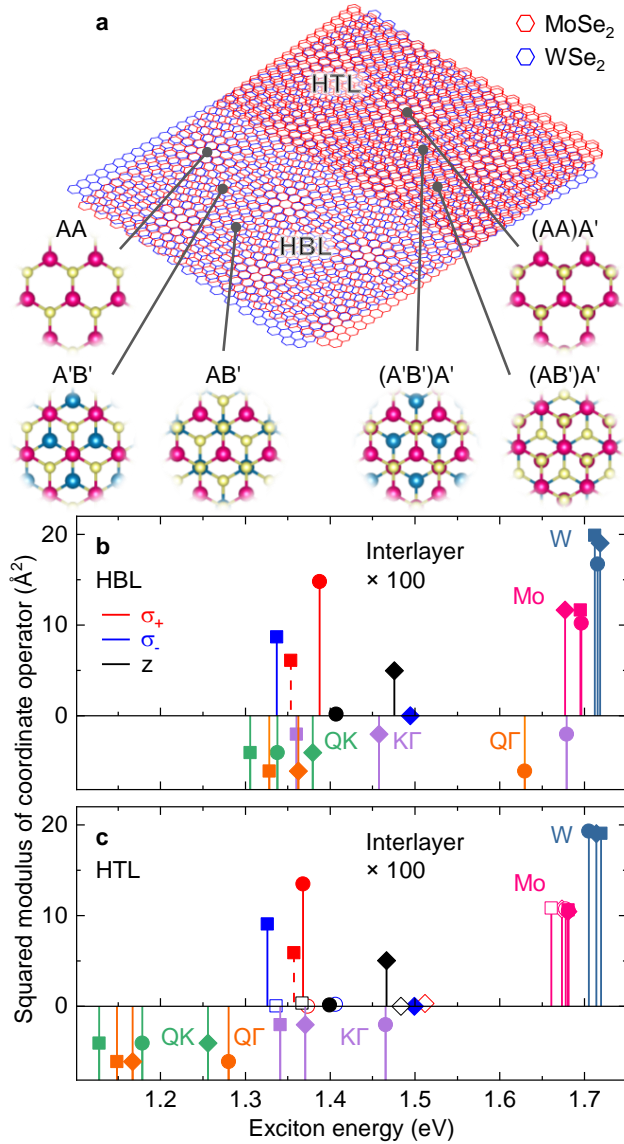


FIG. 2. **Theory of excitons in high-symmetry stackings of MoSe₂-WSe₂ heterobilayer and heterotrilayer.** **a**, Schematics of twisted HBL and HTL MoSe₂-WSe₂ with different high-symmetry stackings. **b** and **c**, Energy and squared sum of coordinate operator (multiplied by 100 below 1.55 eV) for intralayer and interlayer excitons in HBL and HTL, respectively, calculated for three different stackings. Filled squares, circles, and diamonds denote A'B', AA, and AB', and (A'B')A', (AA)A', and (AB')A' stackings in HBL and HTL, respectively. Empty symbols indicate corresponding HTL excitons with electrons residing in the top-most MoSe₂ layer. For zero-momentum KK interlayer excitons (top panels) we indicate the spin configuration by solid and dashed lines for spin-like and spin-unlike states (corresponding to spin-singlet and spin-triplet excitons), and the polarization of the respective exciton emission by red (σ^+), blue (σ^-) and black (in-plane z) colors. The bottom panels show the energy of finite-momentum interlayer excitons in QK (green), $Q\Gamma$ (orange) and KT (violet) configurations without direct radiative transitions.

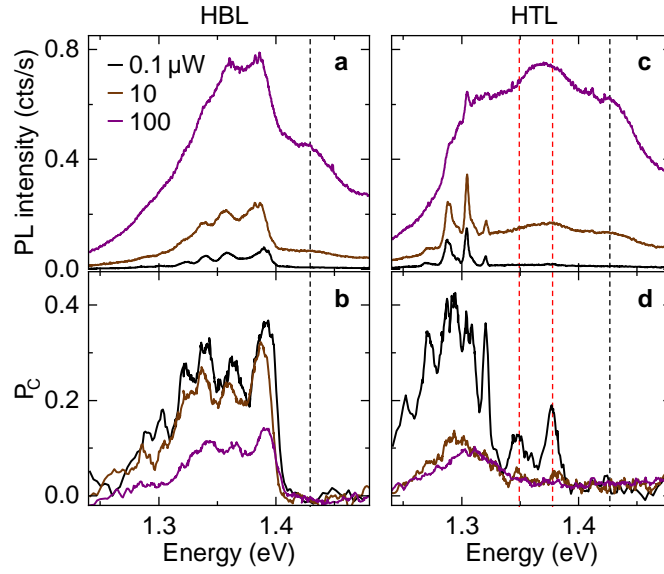


FIG. 3. **Power-dependent photoluminescence and degree of circular polarization of MoSe₂-WSe₂ heterobilayer and heterotrilinear.** **a** and **b**, Photoluminescence spectra and degrees of circular polarization (P_C) for twisted HBL MoSe₂-WSe₂ at 0.1 (black), 10 (brown) and 100 μ W (purple) excitation power. **c** and **d**, Same for HTL MoSe₂-WSe₂. Dashed lines indicate hot luminescence at the higher energy side of the interlayer exciton spectrum with zero (black) and finite (red) P_C .

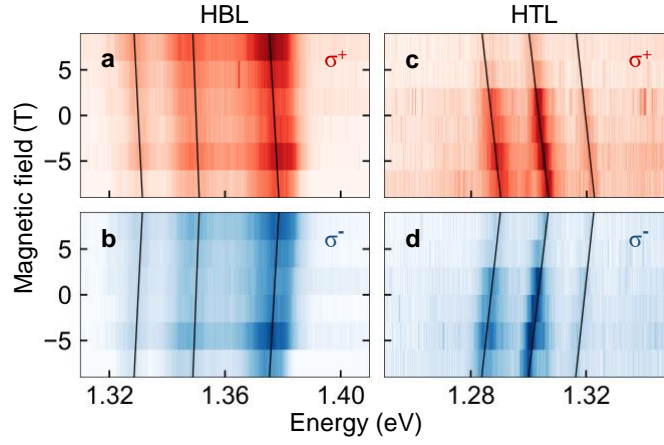


FIG. 4. **Valley Zeeman shift of excitons in MoSe₂-WSe₂ heterobilayer and heterotri-layer.** **a** and **b**, Magneto-luminescence of twisted HBL MoSe₂-WSe₂ for linear excitation and σ^+ (red) and σ^- (blue) circularly polarized detection, respectively. **c** and **d**, Same for HTL MoSe₂-WSe₂. The solid lines show magneto-induced energy shifts of HBL and HTL peaks with g -factors (from high to low energy) and error bars from least-square linear fits of -6.2 ± 0.8 , -4.2 ± 0.8 and -5.5 ± 0.8 , and -12.0 ± 2.0 , -12.0 ± 0.8 and -13.0 ± 0.8 , respectively.

SUPPLEMENTARY INFORMATION:

Moiré excitons in MoSe₂-WSe₂ heterobilayers and heterotrilayers

Michael Förg,¹ Anvar S. Baimuratov,¹ Stanislav Yu. Kruchinin,^{2,3}
Ilia A. Vovk,⁴ Johannes Scherzer,¹ Jonathan Förste,¹ Victor Funk,¹
Kenji Watanabe,⁵ Takashi Taniguchi,⁶ and Alexander Högele^{1,7}

¹*Fakultät für Physik, Munich Quantum Center,
and Center for NanoScience (CeNS),
Ludwig-Maximilians-Universität München,
Geschwister-Scholl-Platz 1, 80539 München, Germany*

²*Center for Computational Materials Sciences,
Faculty of Physics, University of Vienna,
Sensengasse 8/12, 1090 Vienna, Austria*

³*Nuance Communications Austria GmbH, Technologiestraße 8, 1120 Wien*

⁴*Center of Information Optical Technology,
ITMO University, Saint Petersburg 197101, Russia*

⁵*Research Center for Functional Materials,
National Institute for Materials Science,
1-1 Namiki, Tsukuba 305-0044, Japan*

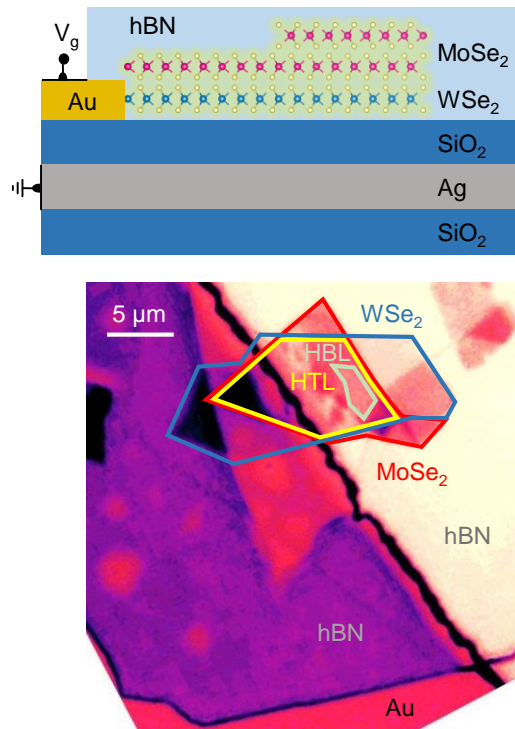
⁶*International Center for Materials Nanoarchitectonics,
National Institute for Materials Science,
1-1 Namiki, Tsukuba 305-0044, Japan*

⁷*Munich Center for Quantum Science and Technology (MCQST),
Schellingstraße 4, 80799 München, Germany*

Supplementary Note 1: Field effect characteristics of MoSe₂-WSe₂ heterostacks

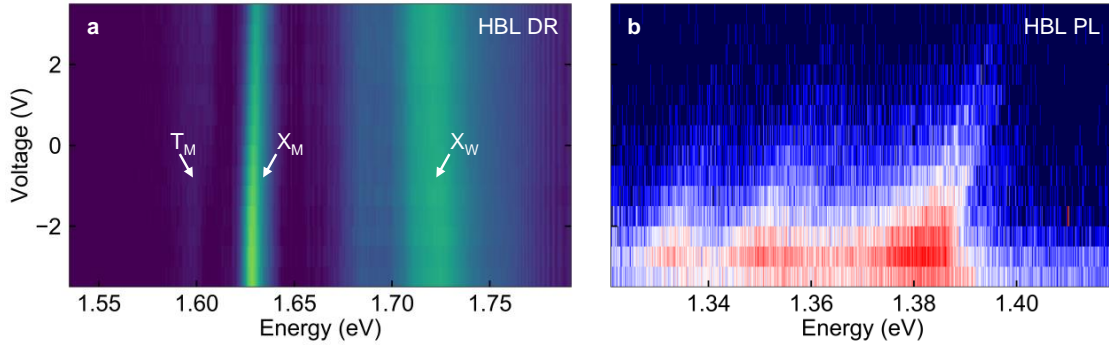
The field effect MoSe₂-WSe₂ heterostructure shown in Supplementary Figure 1 was fabricated by standard mechanical exfoliation using the hot pick-up technique [1]. First, a layer of high quality hexagonal boron nitride (hBN) was picked up with the stamp, followed by MoSe₂ with monolayer (ML) and bilayer (BL) regions, a ML of WSe₂ and a capping layer of hBN. The whole stack was subsequently deposited on a target substrate consisting of a silver (Ag) electrode with a protective layer of 60 nm SiO₂. The doping level in the entire MoSe₂-WSe₂ heterostructure was controlled by the gate voltage (V_g) applied to the Ag electrode in reference to a grounded gold electrode (Au) in contact with the WSe₂ ML.

The charge carrier doping was determined from voltage-dependent differential reflectivity (DR) of intralayer exciton transitions in HBL (Supplementary Figure 2a) and HTL (Supplementary Figure 3a). The corresponding voltage-dependent PL from interlayer excitons is

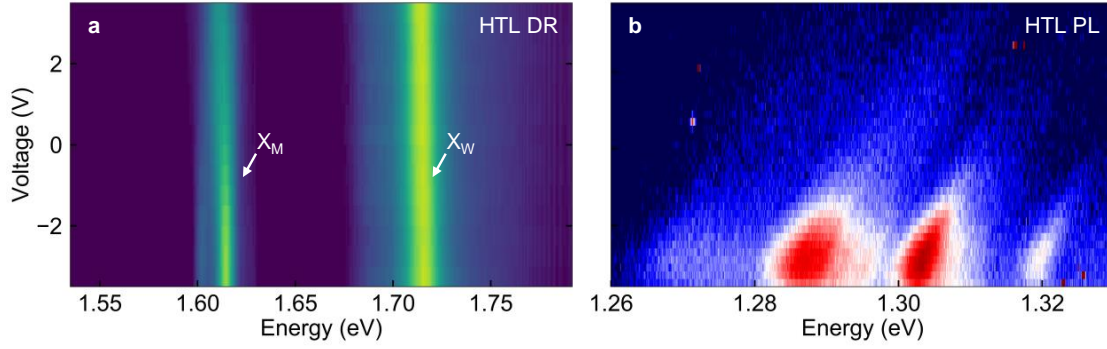


Supplementary Figure 1. Schematic layout (top) and optical micrograph (bottom) of the field effect heterostructure. MoSe₂ and WSe₂ few-layer crystals with monolayer and bilayer regions are delimited in red and blue, the resulting MoSe₂-WSe₂ HBL and HTL regions in light green and yellow, respectively.

shown in Supplementary Figure 2b and Supplementary Figure 3b, respectively. The dominant MoSe₂ and WSe₂ ML features in the DR spectra of both Supplementary Figure 3a and Supplementary Figure 2a are related to the neutral intralayer exciton transitions X_M and X_W , whereas the trion feature T_M in ML MoSe₂ is only weakly expressed. This observation characterizes the heterostacks as very close to the charge neutrality condition throughout the accessible voltage interval explored experimentally. Note that although the peak emission energy and intensity depend on the gate voltage, the overall spectral structure of the interlayer PL exhibits no significant changes. All data of the main text were recorded at 0 V.



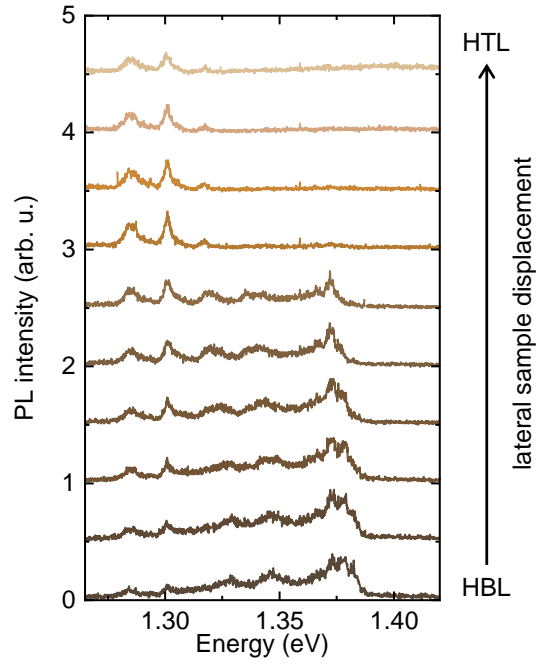
Supplementary Figure 2. **a**, Differential reflectivity (DR) of HBL in the spectral band of intralayer excitons as a function of gate voltage. The labelled features correspond to neutral excitons in ML MoSe₂ and WSe₂ (X_M and X_W , respectively) and a vanishingly weak ML MoSe₂ trion (T_M). **b**, Interlayer exciton PL recorded on the same HBL position. Note that the gate voltage does not change the overall spectral shape.



Supplementary Figure 3. **a**, Differential reflectivity (DR) of HTL in the spectral band of intralayer excitons as a function of gate voltage. The labelled features correspond to neutral excitons in ML MoSe₂ and WSe₂ (X_M and X_W , respectively). **b**, Interlayer exciton PL recorded on the same HTL position. Note that the gate voltage does not change the overall spectral shape.

Supplementary Note 2: Photoluminescence spectra as a function of lateral displacement from MoSe₂-WSe₂ heterobilayer to heterotrilinear

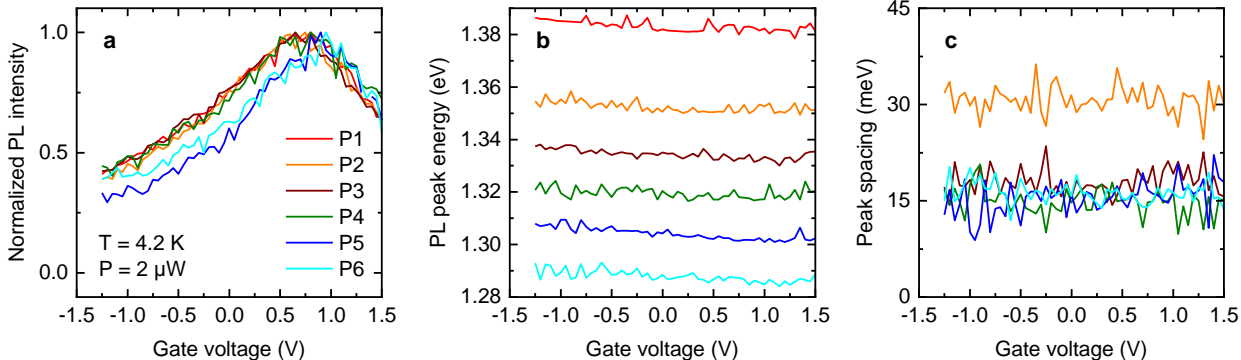
To confirm the reproducibility of the observations as a function of cooling cycles, the sample has been cool-cycled twice, using a low-temperature apochromatic objective with numerical aperture (NA) of 0.63 (with the respective focal spot diameter of $\sim 1.5 \mu\text{m}$) in the first run, and $\text{NA} = 0.81$ (with a smaller spot diameter of $\sim 1.0 \mu\text{m}$) in the second run. All data shown in the main text were recorded with the higher-NA objective. Supplementary Figure 4, with the data from the first run, exemplifies the dependence of the PL spectra on the lateral position. In this experiment, the sample was displaced with respect to fixed confocal excitation and detection spots by moving the heterostructure from the HBL to the HTL region. Evidently, the main features of HBL PL remain robust (peaks in the range $1.32 - 1.39 \text{ eV}$ in the bottom six spectra) before they entirely disappear on the HTL region where red-shifted peaks of HTL PL in the range $1.27 - 1.32 \text{ eV}$ (top four spectra) dominate. The weak yet finite PL cross-talk of HTL features into HBL spectra (that is further suppressed in Fig. 1 of the main text due to the smaller collection spot of the higher-NA objective) stems from insufficient lateral delimitation of the two regions with the objective of lower-NA.



Supplementary Figure 4. PL spectra upon lateral sample displacement from the HBL (bottom) to the HTL region (top).

Supplementary Note 3: Dependence of photoluminescence multi-peak characteristics on gate voltage and excitation power

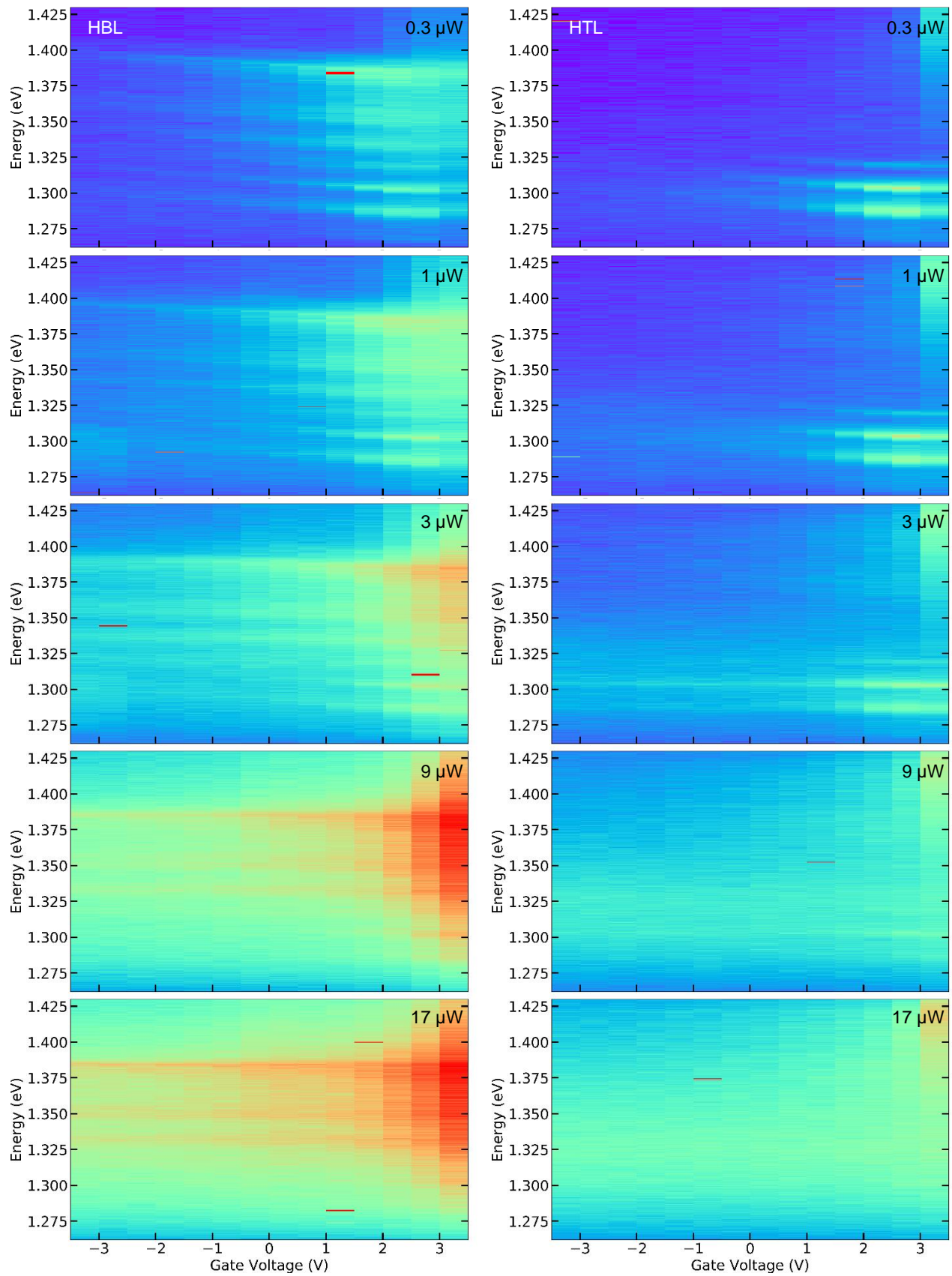
As discussed in the context of Supplementary Figure 3 and Supplementary Figure 2 the multi-peak PL structure is overall robust within the experimentally explored gate voltage range. The quantitative analysis of the spectra as a function of gate voltage recorded on a heterostructure region with contributions from both HBL and HTL stacks (as in the bottom spectrum of Supplementary Figure 4) is shown in Supplementary Figure 5. From the data in Supplementary Figure 5a it is evident that all peaks exhibit similar intensity variations, whereas the data in Supplementary Figure 5b and c confirm that the multi-peak PL structure is preserved throughout the gate voltage range between -1.5 and 1.5 V. In particular, the energy difference of 30 meV between the blue-most peaks (P1 and P2) and 15 meV between all other consecutive peaks is constant in the entire gate voltage range.



Supplementary Figure 5. **a** and **b**, Photoluminescence intensity and energy of peaks in the HBL and HTL spectra recorded on a sample position with contributions from both heterostacks. The peaks are numbered from P1 to P6 with decreasing emission energy. **c**, Energy difference between consecutive peaks as a function of gate voltage.

Qualitatively similar trends were observed as a function of excitation power in Supplementary Figure 6. The left and right panels of Supplementary Figure 6 show voltage-dependent HBL (the red-most peaks are due to cross-talk from the HTL region into the collection spot) and HTL PL for various laser excitation powers. Apart from power-dependent screening the set of data demonstrates that the characteristic multi-peak PL structures of both HBL and HTL are preserved over two orders of magnitude in excitation power. In particular, the intensity of the highest-energy HBL peak is highest at all powers, and the ratio to other

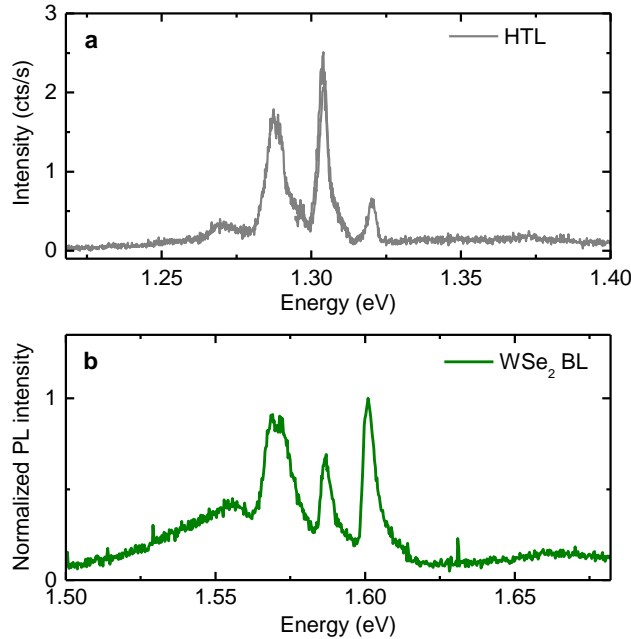
peaks does not reverse down to the lowest excitation power of $0.3 \mu\text{W}$.



Supplementary Figure 6. HBL (left) and HTL (right) photoluminescence as a function of gate voltage at different excitation powers given explicitly in each graph.

Supplementary Note 4: Photoluminescence spectra of MoSe₂-WSe₂ heterotri-layer and native WSe₂ homobilayer

A striking similarity in the PL spectra from MoSe₂-WSe₂ HTL and native WSe₂ BL is evident from Supplementary Figure 9. Native WSe₂ BL exhibits PL emission as phonon-sidebands of momentum indirect QK excitons [2]. The spectra of MoSe₂-WSe₂ HTL and WSe₂ BL feature remarkably similar profiles when red-shifted by the band-offset energy of ~ 280 meV.



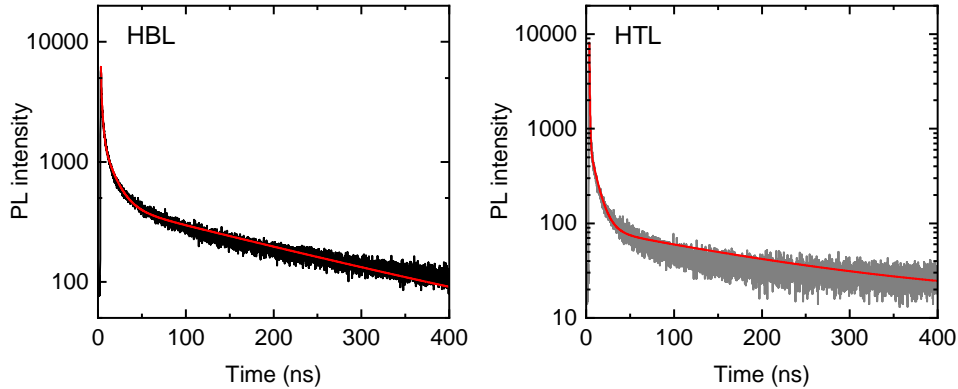
Supplementary Figure 7. **a**, Photoluminescence spectrum of interlayer excitons in MoSe₂-WSe₂ HTL and **b**, native WSe₂ BL encapsulated in hBN. For both measurements the temperature was 3.2 K.

Supplementary Note 5: Time-resolved photoluminescence decay

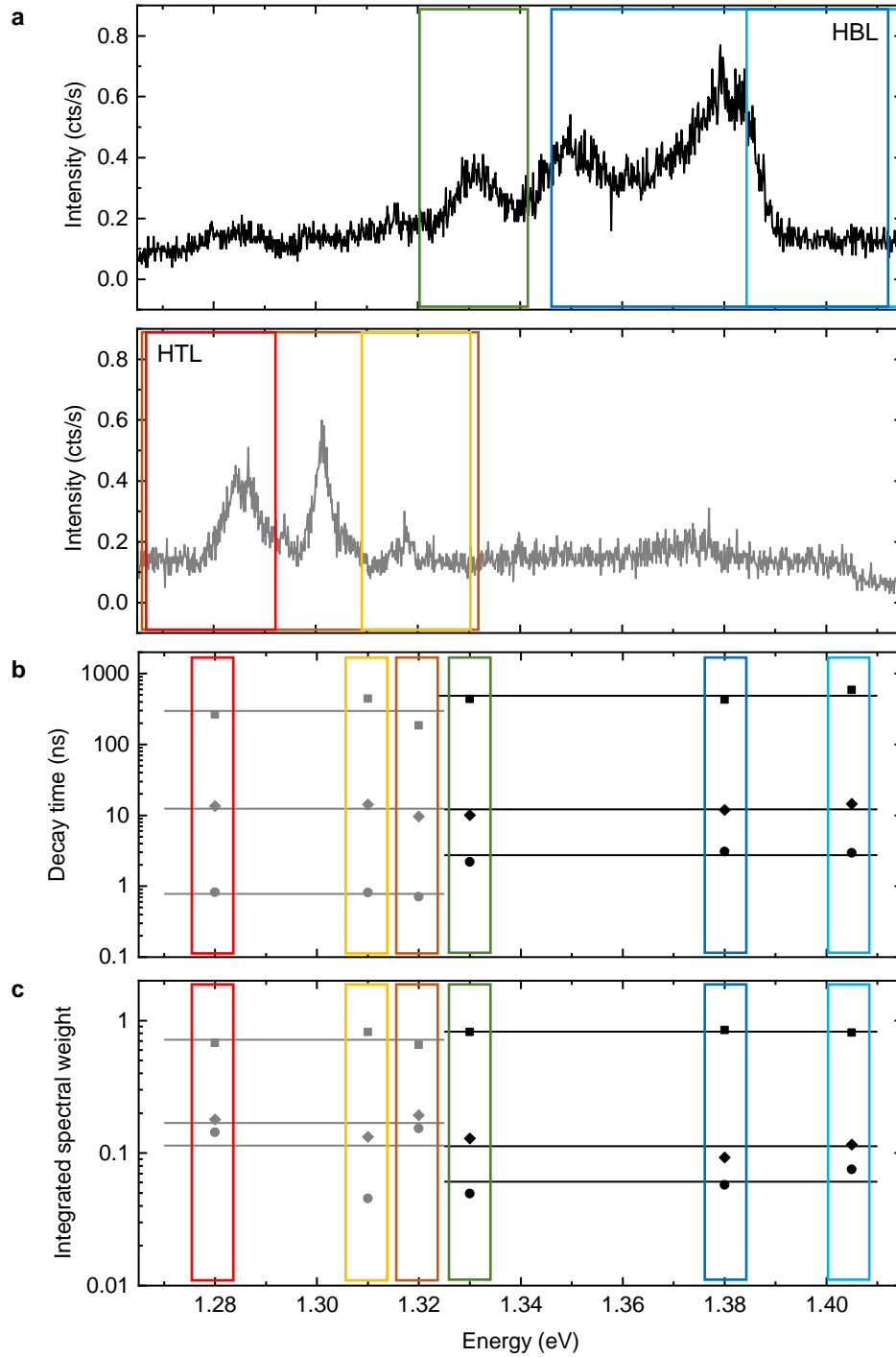
The PL dynamics of HBL and HTL PL were studied with time-resolved PL spectroscopy within various spectral bands. As evident from Supplementary Figure 8 and Supplementary Figure 9, the spectrally structured interlayer exciton emission of HBL and HTL exhibited similar PL decay characteristics. Good approximation to the PL decay was obtained with three exponential decay channels with lifetimes of 3, 12 and 480 ns for HBL and 1, 12 and 300 ns for HTL emission. Remarkably, the contributions of the individual decay channels to the total PL decay varied only marginally across the spectral bands. For both sample

regions, the decay was dominated by the slow decay component (with a weight of 89 and 80% in HBL and HTL, respectively) with contributions of the intermediate and fast decay channels of $\sim 10\%$ (with weights of 8 and 13% for the intermediate and 3 and 7% for the rapid components of HBL and HTL PL decay, respectively).

In Supplementary Figure 9, we summarize the decay data recorded in different spectral bands as indicated by colored regions in the top and bottom panels of Supplementary Figure 9a for HBL and HTL peaks, respectively. The decay times and weights of the three characteristic decay channels, obtained from tri-exponential decay fits within each spectral band, are summarized in Supplementary Figure 9b and c, respectively. The data suggest different PL decay characteristics within HBL and HTL regions with only little dependence on the emission energy for a given heterostack. This observation is inconsistent with lower PL peaks originating from exciton-localizing defects.



Supplementary Figure 8. Photoluminescence decay in MoSe₂-WSe₂ HBL (left) and HTL (right) at zero gate voltage. The excitation was performed at 633 nm and 1 μ W power in the focal spot. The solid red lines show tri-exponential decay as best fits.



Supplementary Figure 9. **a**, Photoluminescence spectra of MoSe₂-WSe₂ HBL (top) and HTL (bottom) with colored spectral windows used to record time-resolved PL decay. **b** and **c**, Decay times and integrated spectral weights for three decay channels of the tri-exponential PL decay obtained from fits to spectrally limited PL bands of HBL (black data points, average values showed by black solid lines) and HTL (grey data points, average values showed by grey solid lines).

Supplementary Note 6: Exciton energies in MoSe₂-WSe₂ heterobilayers and heterotrilayers

Density functional theory (DFT) calculations of MoSe₂-WSe₂ HBL and HTL were performed with the PBEsol exchange-correlation functional [3] as implemented in the Vienna ab initio simulation package (VASP) [4]. Van der Waals interactions were included with the DFT-D3 method by Grimme *et al.* [5] with Becke-Johnson damping [6]. Moreover, spin-orbit interactions were included at all stages. Elementary cells with thickness of 35 Å in the z -direction were used in order to minimize interactions between periodic images. The atomic positions were relaxed with a cutoff energy of 400 eV until the total energy change was less than 10^{-6} eV. Calculations were performed for high-symmetry points of HBL and HTL moiré patterns in R-type stacking as shown in Supplementary Figure 10 on the Γ -centered \mathbf{k} grid of 6×6 divisions with the cutoff energy of 300 eV, with 600 bands for the HBL and 900 bands for the HTL structures. The results for energy gaps and effective masses (in units of free electron mass m_0) are summarized in Supplementary Tables 1 and 2 for HBL and HTL.

Based on these DFT results, we used the Wannier exciton model in the effective mass approximation [7] to calculate the exciton energies E_X for different spin-valley configurations shown in Fig. 2 of the main text, obtained as $E_X = E_g^{\text{DFT}} + E_g^{\text{offset}} - E_b$ from the DFT quasiparticle band gap energy E_g^{DFT} corrected by an offset E_g^{offset} that accounts for an underestimated band gap, and the exciton binding energy E_b . $E_g^{\text{offset}} = 480$ meV was used as a global energy offset for all exciton configurations by placing experimental and theoretical energy positions of KK intralayer excitons of WSe₂ in resonance.

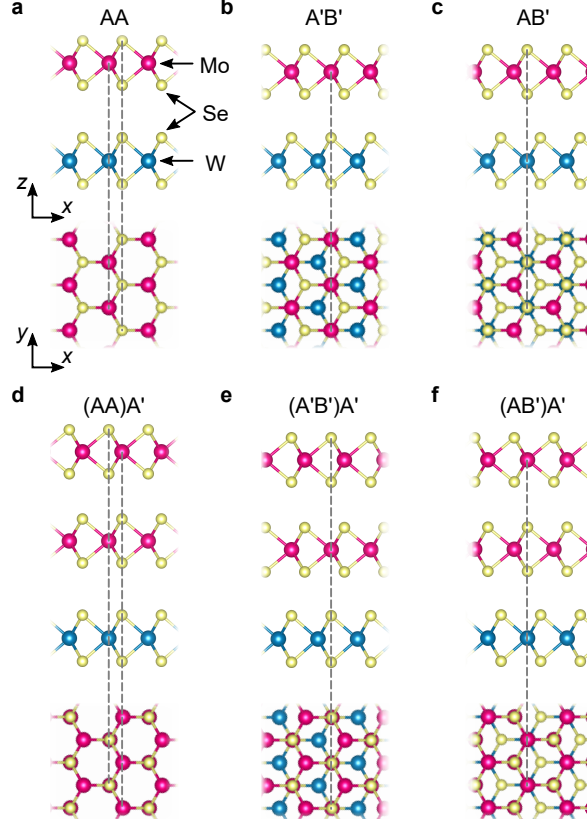
To determine the exciton binding energy we solved the stationary Schrödinger equation of the electron-hole relative motion,

$$\left[-\frac{\hbar^2}{2\mu} \nabla^2 + V(\rho) \right] \psi(\rho) = E_n \psi(\rho), \quad (1)$$

where $\psi(\rho)$ is the radial wave function, $\mu = m_e m_h / (m_e + m_h)$ is the reduced effective mass, m_e and m_h are the effective masses of electron and hole, and $V(\rho)$ the Rytova–Keldysh potential [8, 9] of the form

$$V(\rho) = -\frac{\pi e^2}{2\varepsilon\rho_0} \left[H_0\left(\frac{\rho}{\rho_0}\right) - Y_0\left(\frac{\rho}{\rho_0}\right) \right], \quad (2)$$

with elementary charge e , effective dielectric constant ε , screening length ρ_0 , and Struve and Neumann functions $H_0(x)$ and $Y_0(x)$. The binding energy was obtained as $E_b = -\min(E_n)$



Supplementary Figure 10. High-symmetry stackings in R-type HBL (a–c) and HTL (d–f) MoSe₂-WSe₂.

from the minimal eigenvalue E_n , with $\varepsilon = 4.5$ and $\rho_0 = 1$ nm as parameters for MoSe₂ [10]. Remarkably, this procedure of calculating the exciton energy based on the Wannier model and DFT data yields good quantitative agreement with the computationally expensive simulations based on many-body approximations in HBL case [11]. However, different effective screening in the Coulomb interactions among electrons and holes in different valleys would result in relative energy shifts. A difference of ε by 10% for KK and QK states, for example, would yield an energy shift of about 35 meV. Presently, this uncertainty in the relative energy positions of interlayer exciton states in different valley configurations can not be eliminated from our theory as the valley-dependence of the effective dielectric screening is quantitatively unknown.

Supplementary Note 7: Calculation of exciton g -factors

Our methodology for calculations of exciton g -factors from first principles has been described in detail in [12]. Here, we recapitulate the main steps for determining the g -factors

Supplementary Table 1. Effective masses and energy gaps of HBL MoSe₂-WSe₂ from DFT.

Stacking	Electron			Hole			Energy gap E_g (eV)
	k-point	Layer	$m_e(m_0)$	k-point	Layer	$m_h(m_0)$	
AA	K	W	0.38	K	W	0.47	1.4
	K	Mo	0.67	K	Mo	0.74	1.43
	K	Mo	0.7	K	W	0.47	1.12
	K	Mo	0.67	K	W	0.47	1.1
	Q	Mo/W	0.66	K	W	0.47	1.05
	K	Mo	0.67	Γ	W/Mo	1.36	1.43
	Q	Mo/W	0.66	Γ	W/Mo	1.36	1.38
A'B'	K	W	0.37	K	W	0.44	1.39
	K	Mo	0.63	K	Mo	0.71	1.42
	K	Mo	0.71	K	W	0.44	1.06
	K	Mo	0.63	K	W	0.44	1.04
	Q	Mo/W	0.66	K	W	0.44	1.01
	K	Mo	0.63	Γ	W/Mo	0.85	1.09
	Q	Mo/W	0.66	Γ	W/Mo	0.85	1.06
AB'	K	W	0.39	K	W	0.46	1.4
	K	Mo	0.66	K	Mo	0.72	1.41
	K	Mo	0.73	K	W	0.46	1.2
	K	Mo	0.66	K	W	0.46	1.18
	Q	Mo/W	0.61	K	W	0.46	1.08
	K	Mo	0.66	Γ	W/Mo	0.92	1.20
	Q	Mo/W	0.61	Γ	W/Mo	0.92	1.10

of excitons in different spin and valley configurations in HBL and HTL MoSe₂-WSe₂. The exciton is formed by Coulomb correlations between an occupied state in the conduction band c with the wave vector \mathbf{k}_c and spin z -projection s_c and an empty state in the valence band v with the wave vector \mathbf{k}_v and spin z -projection s_v . In this spin-valley configuration, the exciton g -factor is given by

$$g^{(cv)}(\mathbf{k}_c, \mathbf{k}_v) = g_c(\mathbf{k}_c) - g_v(\mathbf{k}_v), \quad (3)$$

where the g -factor of the electron in band $n = c, v$ is

$$g_n(\mathbf{k}) = g_0 s_n + 2L_n(\mathbf{k}). \quad (4)$$

Here, $g_0 = 2$ is the free electron Landé factor, and the z -component of the orbital angular momentum [13–16] is

$$L_n(\mathbf{k}) = \frac{2m_0}{\hbar^2} \sum_{m \neq n} \text{Im} \left[\xi_{nm}^{(x)}(\mathbf{k}) \xi_{mn}^{(y)}(\mathbf{k}) \right] (E_{n\mathbf{k}} - E_{m\mathbf{k}}). \quad (5)$$

In the summation, the index m runs over all bands excluding the band of interest, $\xi_{nm}(\mathbf{k}) = i\langle u_{n\mathbf{k}} | \partial / \partial \mathbf{k} | u_{m\mathbf{k}} \rangle$ is the interband matrix element of the coordinate operator, $E_{n\mathbf{k}}$ and $u_{n\mathbf{k}}$ are the energy and periodic Bloch amplitude of the electron in band n with wave vector \mathbf{k} .

Supplementary Table 2. Effective masses and energy gaps of HTL MoSe₂-WSe₂ from DFT.

Stacking	Electron			Hole			Energy gap E_g (eV)
	k-point	Layer	$m_e(m_0)$	k-point	Layer	$m_h(m_0)$	
(AA)A'	K	W	0.39	K	W	0.48	1.4
	K	Mo'	0.83	K	Mo'	0.79	1.42
	K	Mo	0.82	K	Mo	0.74	1.42
	K	Mo'	0.58	K	W	0.48	1.11
	K	Mo	0.6	K	W	0.48	1.1
	K	Mo'	0.83	K	W	0.48	1.09
	K	Mo	0.82	K	W	0.48	1.08
	Q	Mo/Mo'/W	0.57	K	W	0.48	0.88
	K	Mo	0.82	Γ	Mo/Mo'/W	0.80	1.21
	Q	Mo/Mo'/W	0.57	Γ	Mo/Mo'/W	0.80	1.01
(A'B')A'	K	W	0.39	K	W	0.46	1.39
	K	Mo'	0.83	K	Mo'	0.75	1.42
	K	Mo	0.81	K	Mo	0.74	1.42
	K	Mo'	0.61	K	W	0.46	1.07
	K	Mo	0.58	K	W	0.46	1.06
	K	Mo'	0.83	K	W	0.46	1.05
	K	Mo	0.81	K	W	0.46	1.04
	Q	Mo/Mo'/W	0.53	K	W	0.46	0.83
	K	Mo	0.81	Γ	Mo/W/Mo'	0.94	1.09
	Q	Mo/Mo'/W	0.53	Γ	Mo/W/Mo'	0.94	0.88
(AB')A'	K	W	0.38	K	W	0.44	1.4
	K	Mo'	0.81	K	Mo'	0.69	1.42
	K	Mo	0.79	K	Mo	0.73	1.4
	K	Mo'	0.63	K	W	0.44	1.21
	K	Mo	0.56	K	W	0.44	1.2
	K	Mo'	0.81	K	W	0.44	1.19
	K	Mo	0.79	K	W	0.44	1.18
	Q	Mo/Mo'/W	0.55	K	W	0.44	0.95
	K	Mo	0.79	Γ	Mo/W/Mo'	0.82	1.11
	Q	Mo/Mo'/W	0.55	Γ	Mo/W/Mo'	0.82	0.89

Using the energy band structure and interband matrix elements of the coordinate operator obtained from DFT we calculate the g -factor for excitons in different spin and valley configurations in HBL and HTL MoSe₂-WSe₂ according to the equations above. The results are summarized in Supplementary Table 3 for momentum-direct KK and momentum-indirect KK' , QK , $Q'K$, KT , and $K'T$ interlayer excitons in HBL (top block) and HTL (bottom blocks) in different stackings of R-type registry.

Supplementary Table 3. Calculated g -factors of interlayer excitons in R-type MoSe₂-WSe₂ HBL (topmost block) and HTL (bottom blocks) in spin-like ($\uparrow\uparrow$) and spin-unlike ($\downarrow\uparrow$) configurations of conduction band electrons in K, K', Q or Q' valleys of MoSe₂ and empty valence band states at K in WSe₂ or at Γ in the hybrid band of MoSe₂-WSe₂. For each spin-valley configuration, the g -factors corresponding to the lower-energy state are shown in bold. For HTL, the upper (lower) block shows $KK, K'K, K\Gamma$, and $K'\Gamma$ excitons with the conduction band electron localized in the lower (upper) MoSe₂ layer, as well as $QK, Q'K, Q\Gamma$, and $Q'\Gamma$ excitons with small (large) hybridization with WSe₂ conduction band states. The sign convention for KK interlayer exciton g -factors is the same as for the KK intralayer exciton in WSe₂; only absolute values are given for momentum-indirect interlayer excitons as well as for direct KK excitons with z -polarized in-plane emission.

Stacking	KK		$K'K$		QK		$Q'K$		$K\Gamma$		$K'\Gamma$		$Q\Gamma$		$Q'\Gamma$	
	$\uparrow\uparrow$	$\downarrow\uparrow$	$\uparrow\uparrow$	$\downarrow\uparrow$	$\uparrow\uparrow$	$\downarrow\uparrow$	$\uparrow\uparrow$	$\downarrow\uparrow$	$\uparrow\uparrow$	$\downarrow\uparrow$	$\uparrow\uparrow$	$\downarrow\uparrow$	$\uparrow\uparrow$	$\downarrow\uparrow$	$\uparrow\uparrow$	$\downarrow\uparrow$
AA	-6.4	11.0	13.0	17.6	9.0	13.3	10.7	15.0	3.6	1.0	3.0	7.6	1.0	3.3	0.7	5.0
A'B'	+5.8	-10.5	13.1	17.8	8.6	13.0	10.6	14.9	4.0	0.7	3.3	8.0	1.1	3.2	0.8	5.1
AB'	6.3	+10.9	13.0	17.6	8.7	12.9	11.0	15.3	3.7	1.0	3.0	7.7	1.3	2.9	1.1	5.3
(AA)A'	-6.3	11.6	12.6	17.9	9.9	14.1	10.1	14.3	3.8	1.5	2.5	7.8	0.2	4.0	0.0	4.2
(A'B')A'	+5.9	-10.8	13.1	17.9	9.5	13.8	10.1	14.4	4.0	0.8	3.2	8.0	0.4	3.8	0.2	4.4
(AB')A'	6.3	+12.2	12.0	18.0	9.6	13.9	10.4	14.6	3.8	2.1	1.9	7.8	0.5	3.7	0.3	4.5
(AA)A'	+12.8	-18.1	6.1	11.4	9.1	13.3	10.9	15.1	2.7	8.0	4.0	1.3	1.0	3.2	0.8	5.0
(A'B')A'	13.1	+18.0	5.9	10.7	8.8	12.9	10.9	15.1	3.2	8.0	4.0	0.8	1.2	3.0	1.0	5.2
(AB')A'	-12.9	18.8	5.5	11.4	9.1	12.9	11.3	15.1	2.8	8.7	4.7	1.2	1.0	2.8	1.2	5.0

SUPPLEMENTARY REFERENCES

- [1] F. Pizzocchero, L. Gammelgaard, B. S. Jessen, J. M. Caridad, L. Wang, J. Hone, P. Bøggild, and T. J. Booth, The hot pick-up technique for batch assembly of van der Waals heterostructures, *Nat. Commun.* **7**, 11894 (2016).
- [2] J. Lindlau, M. Selig, A. Neumann, L. Colombier, J. Förste, V. Funk, M. Förg, J. Kim, G. Berghäuser, T. Taniguchi, K. Watanabe, F. Wang, E. Malic, and A. Högele, The role of momentum-dark excitons in the elementary optical response of bilayer WSe₂, *Nat. Commun.* **9**, 2586 (2018).

- [3] G. I. Csonka, J. P. Perdew, A. Ruzsinszky, P. H. T. Philipsen, S. Lebègue, J. Paier, O. A. Vydrov, and J. G. Ángyán, Assessing the performance of recent density functionals for bulk solids, *Phys. Rev. B* **79**, 155107 (2009).
- [4] M. Shishkin and G. Kresse, Self-consistent GW calculations for semiconductors and insulators, *Phys. Rev. B* **75**, 235102 (2007).
- [5] S. Grimme, J. Antony, S. Ehrlich, and H. Krieg, A consistent and accurate ab initio parametrization of density functional dispersion correction (DFT-D) for the 94 elements H-Pu, *J. Chem. Phys.* **132**, 154104 (2010).
- [6] S. Grimme, S. Ehrlich, and L. Goerigk, Effect of the damping function in dispersion corrected density functional theory, *J. Comp. Chem.* **32**, 1456 (2011).
- [7] G. Berghäuser and E. Malic, Analytical approach to excitonic properties of MoS₂, *Phys. Rev. B* **89**, 125309 (2014).
- [8] L. V. Keldysh, Coulomb interaction in thin semiconductor and semimetal films, *JEPT Lett.* **29**, 658 (1979).
- [9] N. S. Rytova, The screened potential of a point charge in a thin film, *Mosc. Univ. Phys. Bull.* **3**, 18 (1967).
- [10] B. Han, C. Robert, E. Courtade, M. Manca, S. Shree, T. Amand, P. Renucci, T. Taniguchi, K. Watanabe, X. Marie, L. E. Golub, M. M. Glazov, and B. Urbaszek, Exciton states in monolayer MoSe₂ and MoTe₂ probed by upconversion spectroscopy, *Phys. Rev. X* **8**, 031073 (2018).
- [11] R. Gillen and J. Maultzsch, Interlayer excitons in MoSe₂/WSe₂ heterostructures from first principles, *Phys. Rev. B* **97**, 165306 (2018).
- [12] J. Förste, N. V. Tepliakov, S. Yu. Kruchinin, J. Lindlau, V. Funk, M. Förg, K. Watanabe, T. Taniguchi, A. S. Baimuratov, and A. Högele, Exciton g-factors in monolayer and bilayer WSe₂ from experiment and theory, *Nat. Commun.* **11**, 4539 (2020).
- [13] L. M. Roth, B. Lax, and S. Zwerdling, Theory of optical magneto-absorption effects in semiconductors, *Phys. Rev.* **114**, 90 (1959).
- [14] G. L. Bir and G. E. Pikus, *Symmetry and strain-induced effects in semiconductors* (Wiley New York, 1974).
- [15] D. Xiao, M.-C. Chang, and Q. Niu, Berry phase effects on electronic properties, *Rev. Mod. Phys.* **82**, 1959 (2010).

- [16] G. Wang, L. Bouet, M. M. Glazov, T. Amand, E. L. Ivchenko, E. Palleau, X. Marie, and B. Urbaszek, Magneto-optics in transition metal diselenide monolayers, [2D Mater.](#) **2**, 034002 (2015).